Optical wavefront differentiation: wavefront sensing for solar adaptive optics based on a LCD

Dirk Schmidt and Oskar von der Lühe

Kiepenheuer-Institut für Sonnenphysik (KIS)
Schöneckstraße 6, 79106 Freiburg, GERMANY

ABSTRACT

We present the results of our first experimental tests of the concept of an alternative wavefront sensor for extended, incoherent light sources such as the sun. This concept is not associated with subapertures and therefore does not suffer from involved restrictions. In theory, this wavefront sensor also needs very little light from the telescope. The sensor employs a liquid crystal display as used in digital video projectors for masking an image plane in an aberrated telescope. We describe a laboratory setup and an advanced prototype used at the German Vaccum Tower Telescope (VTT), Tenerife.

Keywords: Solar adaptive optics, wavefront sensor, extended source wavefront sensing, Liquid Crystal Display

1. INTRODUCTION

Adaptive Optics (AO) systems compensating atmospheric seeing and offering a nearly diffraction limited resolution are established in everyday observations of the Sun in the visible spectral range. Current AO systems use Hartmann-Shack wavefront sensors (HS-WFS) exclusively to measure the two-dimensional wavefront slope.

A HS-WFS divides the aperture into subapertures using a two-dimensional array of microlenses placed into the collimated beam. These lenses form individual images of the observed object in their focal plane. The motion in each image quantifies the average wavefront slope within the corresponding subaperture. With extended objects showing sufficient contrast, such as the sun, the image motions are determined by cross-correlating the images. To sample the wavefront slope this way, the size of the subapertures has two constraints: first, the dominating wavefront abberation within a subaperture must be tip/tilt. Therefore the size of a subaperture must not be too large. The maximum size is given by the seeing. Second, the subaperture must not be too small, because the image gets blurred by diffraction, making cross-correlation difficult. The latter constraint limits the number of subapertures and with it the sampling of the wavefront slope over the full aperture.

A principle of wavefront sensing applicable for extended objects that does not make use of subapertures, but differentiating the wavefront optically was proposed by von der Lühe.[1] This principle converts the wavefront slope into a fluctuation in intensity in a conjugate plane of the telescope's pupil by manipulating the image of the observed object in the focal plane. The optical wavefront differentiation should need just about 10 % of the telescope's light to operate photon-noise limited on the Sun.[2]

2. PRINCIPLE OF OPTICAL WAVEFRONT DIFFERENTIATION

Figure 1 shows the basic principle of an optical differentiation wavefront sensor (OD-WFS). The sensor consists of two lenses and an amplitude modulating mask which are set up as a spatial filter for pupilplane frequencies. The intermediate image or Fourier plane is masked in a way, that the wavefront slope along a certain direction is coded in the intensity of the pupil image. This direction is defined by the mask which is computed from the observed object's image taken by a camera in a separate optical path (not shown). Using two linearly independent (e. g. orthogonal) masks, the complete two-dimensional information about the wavefront gradient is available as pupil intensity maps. In figure 2, a sample image of solar granulation is overlaid with a corresponding mask. If the image moves horizontally due to a wavefront tilt, the overall intensity in the image plane de- or increases with respect to the direction, presuming the shift being not too large. The intensity variation is about ten times smaller when moving the image up and down. Decreasing or increasing the total intensity in the image plane also de- or increases the flux in following pupils. This idea can be easily extended from full aperture wavefront tilt to local tilts which then cause local variations of intensity in the pupils. In principle, the mask is static, but with the Sun it has to be updated roughly every minute because of the evolution of the solar structure.

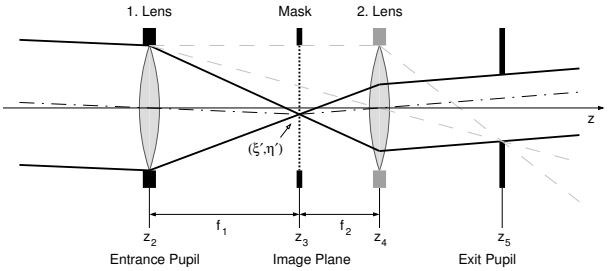

Figure 1. Basic setup of the OD-WFS. The mask modulates the image plane in a way, that the directional wavefront slope in the entrance pupil is coded in the intensity of the following pupil image.

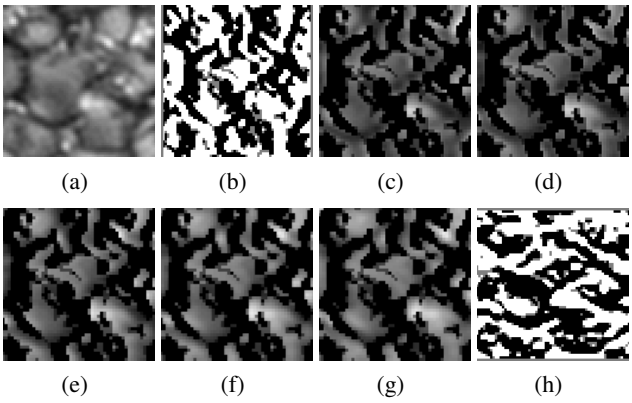

Figure 2. (a) is a sample image of an $10'' \times 10''$ square of solar granulation. (b) is the horizontal mask computed from (a) according to Eq. (3) and sampled down to basically two transmission levels. (c)-(g) are the products of (a) shifted by -7, -3, 0, +3 and +7 pixels to the right and (b). The overall intensity of (c)-(g) increases from 0.88, 0.90, 1.00, 1.10 up to 1.12. (h) is the vertical mask.

2.1. Physical Description

The intensity distribution in the pupil plane conjugate z_5 of figure 1 can be found analytically by using the theory of linear, shift invariant systems and Fourier-optics:[3] The complex amplitude of the electric field $u_5(x, y; \xi, \eta)$ in this plane caused by a point source on the object at the angle (ξ, η) measured from the optical axis can in general be expressed by the two-dimensional convolution

$$u_5(x, y; \xi, \eta) = u_2 \left(-\frac{f_2}{f_1} x, -\frac{f_2}{f_1} y; \xi, \eta \right) * M \left(-\frac{f_1}{f_2} x, -\frac{f_1}{f_2} y \right). \tag{1}$$

$M(x, y)$ is the impulse response of the system and is given by the Fourier-transform of the complex amplitude transfer function which corresponds to the mask's transmission $m(\xi, \eta)$ here. $u_2(x, y; \xi, \eta)$ is the complex electric field amplitude in plane z_2 caused by the point source at (ξ, η). The magnification factor f_1/f_2 is the ratio of the focal lengths of the lenses 1 and 2 in figure 1. A detailed derivation of equation (1) can be found in reference 1. The overall intensity in the pupil plane conjugate z_5 arised by the entire object is given by the sum of all point source intensities

$$I_5(x, y) = \iint |u_5(x, y; \xi, \eta)|^2 \, \mathrm{d}\xi \, \mathrm{d}\eta. \tag{2}$$

To let $I_5(x, y)$ represent the horizontal wavefront slope in z_2, von der Lühe suggests[1] to compute the mask transmittance from the image $I(\xi, \eta)$ via

$$m^+(\xi, \eta) = B + C \left[I\left(\xi + \Delta,\, \eta\right) - I\left(\xi - \Delta,\, \eta\right) \right]. \tag{3}$$

B and C are constants limiting $m^+(\xi, \eta)$ between 0 and 1. Equation (3) describes the numerical and normalized, horizontal derivative of the object structure. The shift Δ should not be larger than the correlation length of this structure ($\approx 1.5''$ for solar granulation). Using this mask, von der Lühe approximates equation (2)

$$I_5^+(x, y) \propto \overline{I}_{\text{Object}} + \text{const.} \, \left[\phi(x, y) - \phi\left(x - \delta_0, y\right) \right], \tag{4}$$

for small wavefront abberations ($\phi(x, y) - \phi\left(x - \delta_0, y\right) \ll \lambda/4$). $\phi(x, y)$ denotes the wavefront error phase at the point (x, y) in the pupil plane z_2 and $\overline{I}_{\text{Object}}$ represents the object's mean intensity. Thus, the intensity in the pupil image is given by a constant offset and the error phase difference of two points being separated by δ_0 in horizontal direction. To compensate this offset which would be effectively a tip/tilt signal (especially when the intrinsic object brightness varies, or clouds pass by), one can place the inverted mask

$$m^-(x, y) := 1 - m^+(x, y) \tag{5}$$

in a similar but separate optical path and record its pupil intensity $I_5^-(x,y)$ simultaneously. The difference of these two intensities is directly proportional to the phase difference:

$$I_5^+(x,y) - I_5^-(x,y) \propto \phi(x,y) - \phi\left(x - \delta_0, y\right) \tag{6}$$

The distance δ_0 depends on Δ and on the correlation length of the object. If Δ equals this correlation length, then $\delta_0 = 2\Delta/\left|\Delta\right|^2$ and the optical wavefront differentiation is most efficient. All discussions above can analogously be applied for the vertical direction.

Von der Lühe was able to show, that the mask's transmission does not need to be continuous but can be sampled down to three levels without compromising the performance of this sensor. This is of special importance when using liquid crystal displays (LCDs) to carry the mask as described in the next section.

3. LABORATORY DEMONSTRATION

In order to demonstrate the principle of the optical wavefront differentiation experimentally, we first built a laboratory setup in which we directed an OD-WFS to an artificial sun and introduced static aberrations.

3.1. Laboratory Test Setup

The scheme of the laboratory setup is sketched in figure 3. A small section of the solar surface, typically a 10 arcsec square, is displayed on LCD_1 and imaged to infinity by the collimator lens. The plain wavefront emanating from the collimator is aberrated statically with a deformable mirror (DM) and enters the OD-WFS at Lens $\mathrm{L_I}$. This lens reimages the solar surface on a scale of 1:1 in its focal plane. In this plane, LCD_2, displaying the mask, is placed. Lens $\mathrm{L_{II}}$ collimates the masked image plane and images the pupil, which is defined by an aperture stop in front of the DM. The pupil image intensity is recorded by a CMOS-camera.

To identify the complete wavefront aberration via optical differentiation, we first display the horizontal mask on LCD_2 and capture a number of frames with the camera and average them. Then we invert the mask and let the camera record again. Finally we subtract the two average images to get the horizontal slope of the wavefront aberration. The same procedure is repeated with the vertical mask to acquire the vertical wavefront slope.

A Twyman-Green interferometer (not shown) is used to measure the shape of the DM as a reference for the introduced wavefront aberration. This reference is used for benchmarking the optical wavefront differentiation.

The masks are computed from the sample image displayed on LCD_1 following equation (3) with $\Delta = 0.16''$. Because LCDs do not only change the amplitude, but do also change the phase of the transmitted light, we sample down the transmittance of the mask to basically two levels: The median value of the mask is set to 50% gray, pixels with values greater than the median are set to white (transparent) and the rest is set to black (opaque). With this method of down sampling, it is ensured that overall transmittance of the mask is preserved best while inverting. A few gray pixels (local phase modification!) should not affect the performace of the sensor.

3.1.1. Technical details

The two LCDs (Epson L3D07H, 1284×724 pixels, 12 µm pixels with microlenses) were dismounted from a commercial digital video projector (Hitachi Illumina PJ-TX100) and have been reconnected to the projector's mainboard using a custom made extension cord. This solution has two major benefits: first, commercial video projectors are available for 1,000 to 2,000 EUR while development kits are much more expensive; furthermore we can easily display images on the LCDs just by using the graphics system of a PC equipped with a Digital Visual Interface (DVI). We use *XFree86* 4.3 on a 866 MHz Pentium III PC with a *NVIDIA GeForce FX 5200* graphics processing unit, running on Linux 2.6.8 and the *nvidia* XFree86 driver module.

Because colors are reproduced with a LCD-projector by using the additive color model, such projectors employ three identical monochrome LCD panels displaying the red, green and blue (RGB) components of an image separately. Dichroic optics are used to illuminate the LCDs with their respective colors and to merge the RGB-components afterwards.[4] In order to display the solar surface merely on LCD_1 which is the panel of the green channel, its RB-components have to be set to maximum. Analogously, the masks are displayed only on the red-channel LCD_2 by setting their GB-components to maximum.

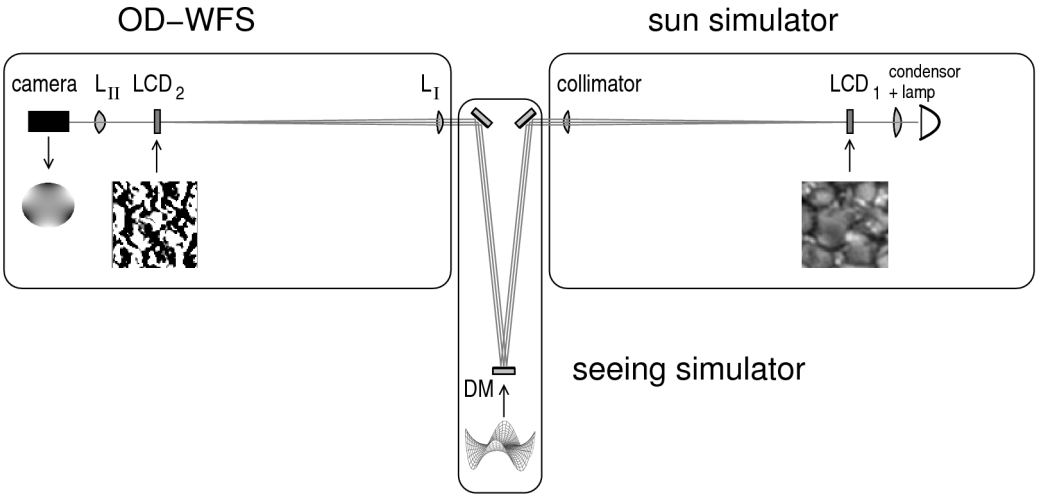

Figure 3. Sketch of the laboratory OD-WFS test setup (light is propagating from right to left). The OD-WFS is pointed at an artificial sun, realized by a collimated image of solar surface on LCD_1. The deformable mirror (DM) introduces static seeing which is to be sensed by the OD-WFS. An aperture stop ($D = 7$ mm) defining the pupil is directly located in front of the DM. The focal lengths of the lenses are: $f_{\mathrm{collimator}} = f_{\mathrm{I}} = 500$ mm, $f_{\mathrm{II}} = 100$mm. The LCDs' polarizers are not shown explicitly.

We implemented a program, utilizing the *Simple DirectMedia Layer*[*] software library, that reads an image file containing the solar surface, computes the mask and displays them both as described on the video projector.

The ultra-high-pressure mercury-vapor lamp deployed for illuminating LCD_1 was also dismounted from the projector, installed in a custom made air cooled case and reconnected to the projector. To get rid of the vast thermal power of this lamp and to pre-polarize its light, we used reflective optics (Brewster's angle) and heat absorbing glass which are not shown in figure 3.

The deformable mirror is a 15 mm, 37 channel, micromachined membrane deformable mirror (known as *OKO mirror*) manufactured by *Flexible Optical B.V.*, The Netherlands. The Twyman-Green interferometer is a *µPhase* compact digital interferometer system by *Fisba Optik*, Switzerland.

3.1.2. Optical considerations

Diffraction caused by LCD_2 duplicates the pupil image at the camera plane. To avoid overlapping of those images, the focal length of $\mathrm{L_I}$ and the aperture stop in front of the DM have to be chosen such that its Airy disc covers at least two pixels at LCD_2. This is the case if

$$D < \frac{\lambda f_{\mathrm{I}}}{p} \tag{7}$$

is satisfied, where D is the diameter of the stop, f_{I} the focal length of $\mathrm{L_I}$ and p the center-to-center pitch of the LCD pixels. We used a focal length of 500 mm for the collimating lens and the reimager $\mathrm{L_I}$, 100 mm for $\mathrm{L_{II}}$, and $D = 7$ mm.

3.2. Data Acquisition and Evaluation

For benchmarking the optical wavefront differentiation, we compared the differences of pupil image intensities to the actual slopes of the deformable mirror.

We decomposed the shape of the deformable mirror, which is scanned by the interferometer, into Zernike coefficients and computed its horizontal and vertical slopes using the derivative matrices introduced by Noll.[5] The Zernike coefficients of these slopes were compared with the Zernike coefficients of the corresponding differences of pupil intensities (Eq. (6)) recorded by the camera. The Zernike decomposition was computed using the linear least squares fit routine (see sec. 15.4 in Ref. 6) from the GNU Scientific Library (GSL)[†].

[*] http://www.libsdl.org

[†] http://www.gnu.org/software/gsl/

To be able to roughly produce single Zernike modes within the aperture stop, we estimated a reconstruction matrix for the DM. This was done by utilizing the Poisson equation for the vertical deflection of the membrane mentioned in Eq. (1) in Ref. 7 and approximating the load on the membrane being proportional to the voltage distribution of actuator electrodes.

As mentioned before, we use a Twyman-Green interferometer to scan the deflection of the membrane of the DM at the applied voltage patterns. Unfortunately the test beam of the present interferometer system had a diameter of 50 mm, while the pupil's diameter was 7 mm. Hence we could acquire only about 400 to 500 data points within the aperture leading to several difficulties when decomposing the mirror shape into Zernike polynomials. The greatest issue was arranging the unit circle of decomposition on the data points because the edge of the stop is blurred and frayed in the interferogram. Finally we decomposed each sampled mirror shape within four separate circles with their centers forming a quadcell containing the real center of the aperture and averaged all four Zernike coefficients of each order. We had to realize that the four coefficients of a given order are significantly different with respect to the estimated fit error. We decided to specify the error of their average by their standard deviation as an estimation. The estimation error of decomposing the pupil intensity differences is negligible.

3.3. Results

To see, whether the pupil intensities are actually correlated somehow with the arriving wavefront, we introduced static abberations like defocus, astigmatism, and trefoil individually with the deformable mirror. Take a look at figure 4 where the measured pupil image intensity differences are printed to get a first impression of the effect of alternating the sign of the introduced wavefront aberration. The peak-to-valley amplitudes used were approx. 530 nm for the tilt, 650 nm (positive) and 200 nm (negative) for the defocus, and 315 nm for the trefoil. The intensity differences in the first row of figure 4 obviously indicate the horizontal tilt. In the second row, at least the intensity differences for the horizontal direction indicate the defocus. The intensity differences in the third row look similar to astigmatisms which are actually the slopes of a trefoil.

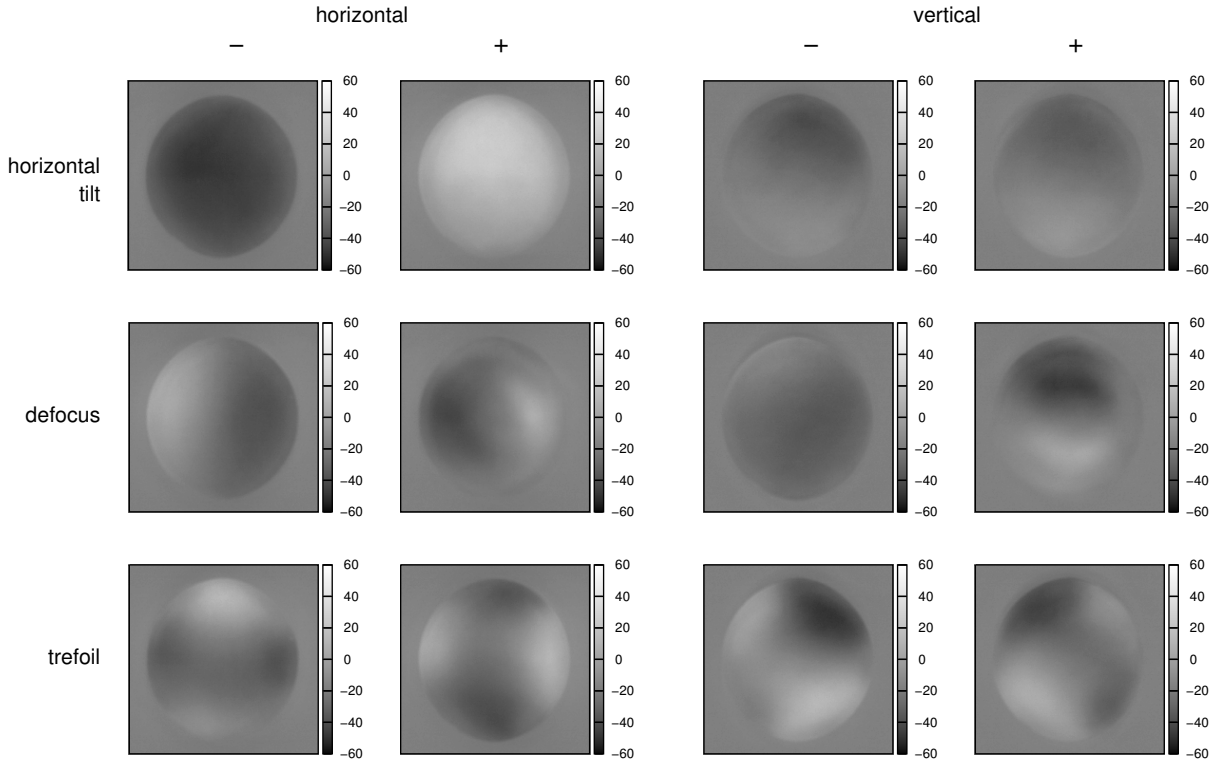

Figure 4. Pupil image intensity differences at various aberrations (tilt, defocus and trefoil) with alternating sign. In the first two columns, the differences for the horizontal mask direction is shown, and the last two columns show the differences for vertical direction.

For a more quantitative impression of the performance of the setup refer to figures 5 and 6 where the Zernike coefficients of the intensity differences are compared to the coefficients of the DM's slopes. The typical orders of the aberrations were found. However, some coefficients of other orders did not correlate with the DM shape.

We did much more tests done with this setup than presented in this article. All our tests and the results can be found in reference 8.

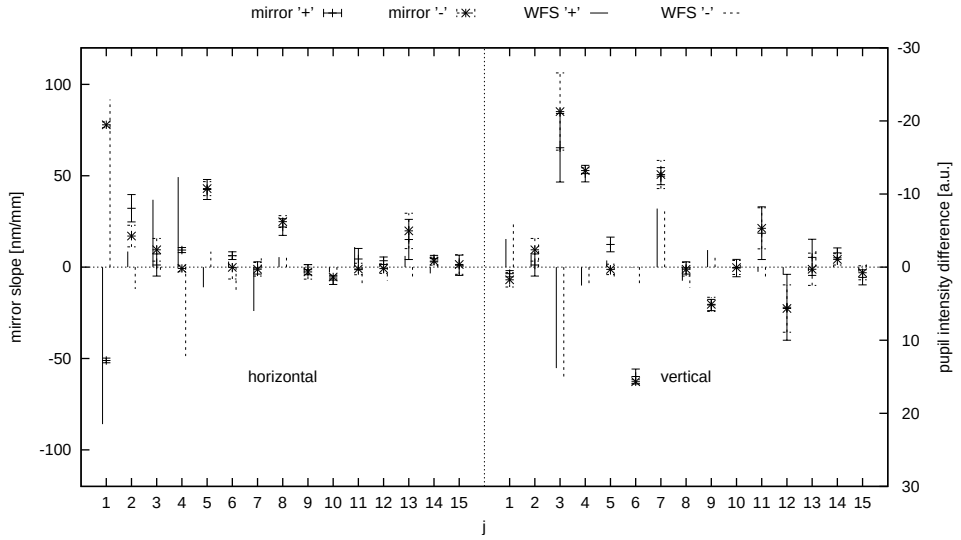

Figure 5. Zernike decomposition of the pupil image intensity differences and of the slopes of the shape of the DM. The horizontal data are plotted on the left, and the vertical data on the right. The DM was driven to a horizontal tilt ($\approx$ 530 nm PV) with different signs ($+/-$). The coefficients of the orders $j = 1; 2; 4; 11$ of the horizontal slope perform parallel in the intensities as well as in the mirror shape. For $j = 3$ the coefficients perform reverse. However, the slight variation for $j = 5$ and $j = 7$ in the intensity difference is not found in the horizontal mirror slope. The coefficients of the vertical dataset show no significant variation when flipping the sign of the aberration.

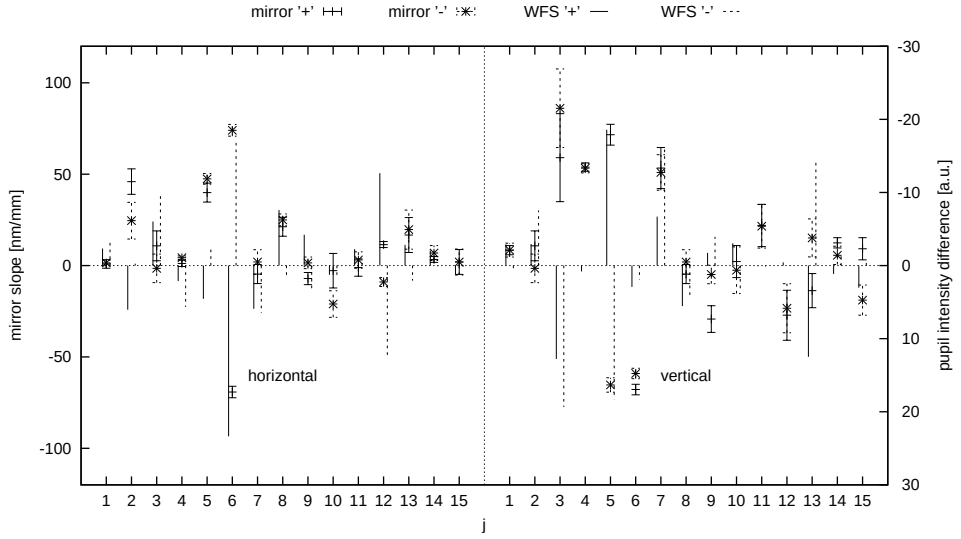

Figure 6. Zernike decomposition by analogy with Fig. 5. Here, trefoil aberrations ($\approx$ 315 nm PV) with different signs were cast to the DM. The distinctive orders of the mirror slopes are $j = 6$ and $j = 12$ and accordingly $j = 5$ and $j = 13$. The same orders are distinctive in the intensity differences.

4. DEMONSTRATION AT THE VACUUM TOWER TELESCOPE

Encouraged by the results achieved with the laboratory setup, we designed a wavefront sensor setup to be tested with the real Sun at the German Vacuum Tower Telescope (VTT) on Tenerife, Spain.

4.1. Prototype Setup

The OD-WFS setup for use at the VTT was designed to enable capturing of the four pupil intensities (two masks in both horizontal and vertical direction) simultaneously with a single shot of one camera. Furthermore no light should be wasted by polarizers. Refer to figure 7 for a schematic sketch of this setup. The VTT forms an image of the solar surface in its focal plane. A square field stop in this plane limits the field of view to approximately 10 arcsecs. The solar image is relayed to a LCD-panel by 4-f-configuration of the lenses 1 and 2. Between these two lenses, a Wollaston prism is placed. This prism splits the light into two beams which are orthogonally polarized. This way, two separate images of the solar surface are formed side by side on the LCD. The vertical and the horizontal masks are displayed congruently with the two solar images on the LCD. There are no polarizers in front and in behind of the LCD-panel, thus the masks are not yet realized as an opacity map. But since LCD-pixels rotate the polarization of light depending on the applied voltage, the mask is realized as a map of polarization rotation of $0°$ or $90°$. Another Wollaston prism (orthogonally orientated to Wollaston 1) is located behind the LCD-panel. This prism separates the light traveling through polarization rotating LCD-pixels from light traveling through non-rotating pixels again into two divergent beams. Hence it realizes the mask and the inverted mask simultaneously as opacity maps but separated into two beams for each mask direction. The following lens forms four images of the telescope's pupil on a fast CCD-camera. The pupil image pair on the left corresponds to the vertical wavefront slope and the pair on the right corresponds to the horizontal wavefront slope. The difference of each pair finally represents the wavefront slope in the corresponding direction, according to equation (6).

Within this setup, no photon is lost to polarizers and each photon (disregarding normal extinction due to the optical components) accounts for wavefront sensing. The image of the solar surface used to compute the masks is taken by a camera in a separate optical path and is not shown in figure 7. The horizontal and vertical masks are computed as described in section 3 from a long term exposure of the solar surface of a few seconds to average the atmospheric seeing. The LCD-panel and the video projector of the laboratory setup were re-used for this setup and the optics were mounted on a dedicated micro-optical bench for easy installation at the VTT. To minimize potential chromatic effects on the polarization rotation of the LCD, we put a broadband blue filter glass (Schott BG5) into the optical path. We chose a blue glass, because the contrast of solar granulation is highest in this wavelength regime.

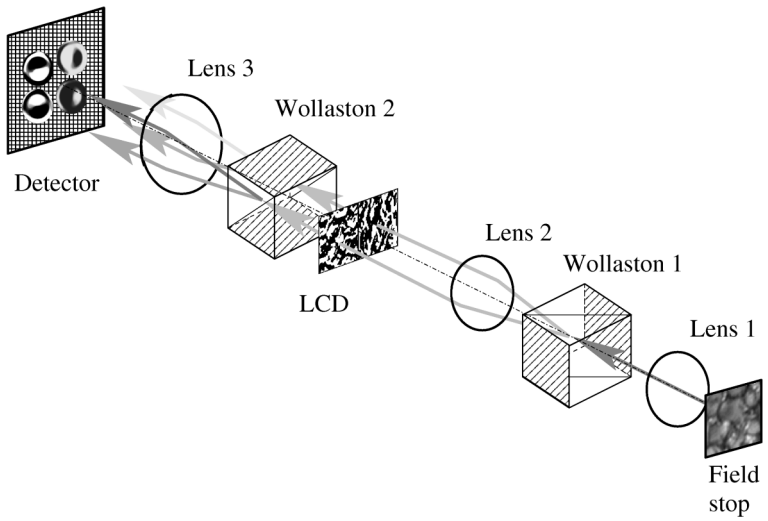

Figure 7. Schematic sketch of the OD-WFS test setup for use at the Vacuum Tower Telescope (VTT).

4.2. Data Acquisition

To demonstrate this realization of an OD-WFS we directed the VTT to the sun compensating atmospherical seeing with the Kiepenheuer Institute Adaptive Optics System (KAOS)[9] running and reintroducing well-known static aberrations in form of Zernike modes with the deformable mirror of KAOS. The pupil images captured by the camera were calibrated with the images captured while the DM was flattened. Afterwards, the difference of two pupil images corresponding to the same mask direction is computed. The reintroduced aberrations probably exhibit an residual error of approximately 10% RMS to analytical Zernike modes.

4.3. Results

4.3.1. Tests with a US Airforce target

We first inserted an static US Airforce target (Fig. 8) into the prime focus of the VTT and used this pattern as the object structure.

Defocus Figure 9 shows the pupil intensity differences with defocus aberrations at ± 250 nm RMS. The horizontal and vertical slopes of the negative defocus are well detected in form of a horizontal or vertical gradient in intensity difference (Fig. 9 (b)), respectively. However, the intensity differences corresponding to the positive defocus (Fig. 9 (a)) do not show the inverse gradients as one would rather expect.

Astigmatism In figure 10 the intensity differences with astigmatism aberrations at ± 250 nm RMS are printed. Analytically, the horizontal slope of a astigmatism aberration is given by a vertical gradient, and the vertical slope is given by a horizontal gradient. In figure 10 one can recognize this gradients which flip with altering the sign of the astigmatism.

(a) USAF target (b) horizontal mask (c) vertical mask

Figure 8. Reference image of an USAF target in the focal plane of the VTT and the corresponding horizontal masks to be displayed on the left side of the LCD. The field of view is $10'' \times 10''$.

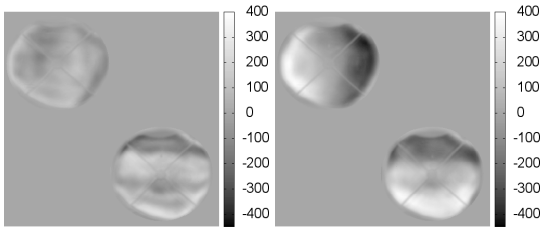

(a) (b)

Figure 9. Pupil intensity differences with defocus aberrations at $+250$ nm RMS (a) and -250 nm RMS (b). The left pupil represents the horizontal wavefront slope and the right pupil represents the vertical slope. The spider seen in the pupil images is the mounting of a mirror used for guiding the telescope. The pupil is not circular because of the coelostat nature of the VTT.

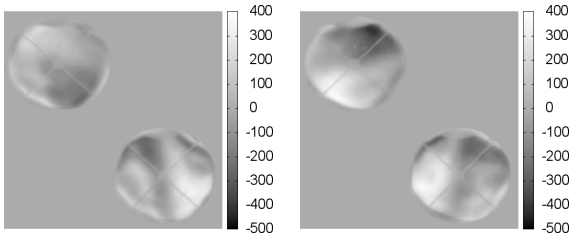

(a) (b)

Figure 10. Pupil intensity differences with astigmatism aberrations at $+250$ nm RMS (a) and -250 nm RMS (b).

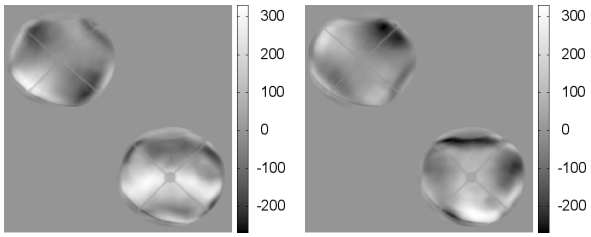

(a) (b)

Figure 11. Pupil intensity differences with trefoil aberrations at $+150$ nm RMS (a) and -150 nm RMS (b).

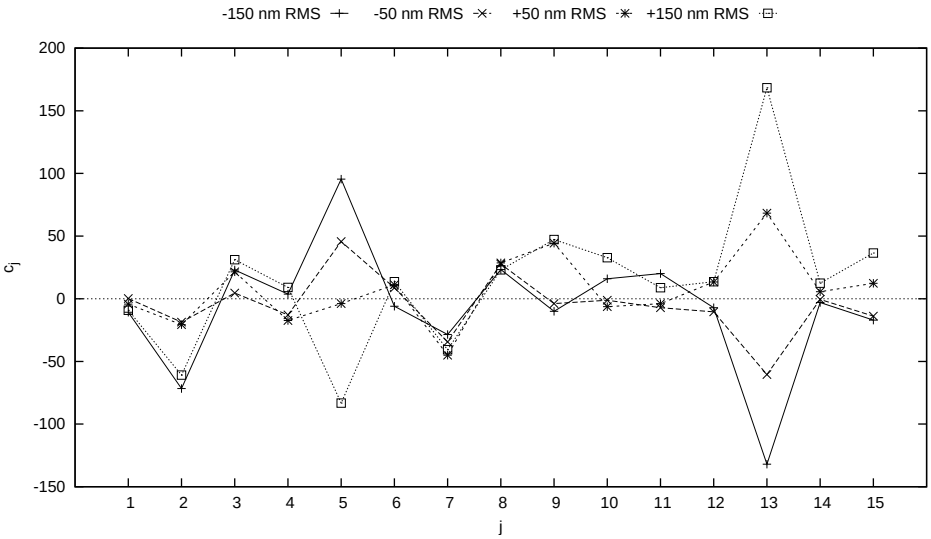

Figure 12. Zernike decomposition of horizontal intensity differences with trefoil aberrations at ± 50 nm and ± 150 nm RMS.

Trefoil The intensity differences captured with trefoil aberrations at ± 150 nm RMS are shown in figure 11. The analytical slope of the trefoil aberration is given by a astigmatism (saddle). The saddle of the vertical slope is equal to the vertical one, but rotated by 45°. This is well represented in the intensity differences shown in figure 11.

In figure 12 the Zernike decomposition of the intensity differences corresponding to the horizontal mask with trefoil aberrations of various amplitudes is shown. The fifth Zernike order shows a strong dependence on the amplitude of the trefoil aberration. This is expected because this is the appropriate coefficient in the analytical derivative of this trefoil. The origin of the strong answer in the 13th Zernike order is not understood since it does not appear in the analytical derivative of trefoil. Maybe this is an artifact of the decomposition within the non-circular pupil.

4.3.2. Tests with solar structure

The same procedure as in section 4.3.1 was repeated using a sunspot as observed object structure and normal solar granulation.

Sunspot The intensity differences when observing the sunspot (Fig. 13) and introducing trefoil aberrations into the optical path are shown in figure 14. The intensities are rotated by 45° compared to figure 11 because the introduced trefoil was rotated by 30°. Again a astigmatism like pattern occurs in the intensity differences which flips with inverting the sign of the introduced aberration. But opposed to figure 11, the horizontal and vertical intensity differences look similar and are not rotated by 90° against each other. To understand this, take a look at the masks shown in figure 13. Due to the diagonal structure of the sunspot in the field of view, the horizontal mask and the vertical mask look similar and no master direction is formed like in figure 2 (b) and (h).

Solar granulation In figure 16 the intensity differences when observing solar granulation (shown in Fig. 15) and introducing trefoil aberrations into the optical path are shown. The signal level dramatically decreases and it is hardly possible to distinct various introduced wavefront aberrations.

5. CONCLUSIONS

We have experimentally demonstrated the principle of an optical-differentiation wavefront sensor (OD-WFS). We also have proposed and tested the optical principle for a light efficient design of a OD-WFS for use at a solar telescope. This design employs two Wollaston prisms instead of two polarizing films such that no light is lost apart from normal instrumental

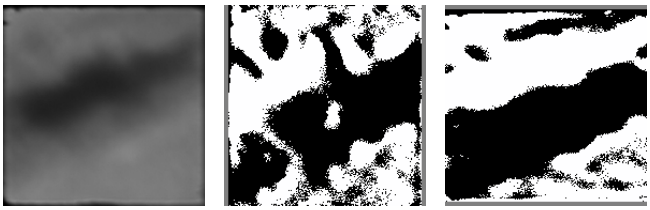

(a) (b) (c)

Figure 13. An observed sunspot (a), the horizontal (b) and the vertical (c) mask.

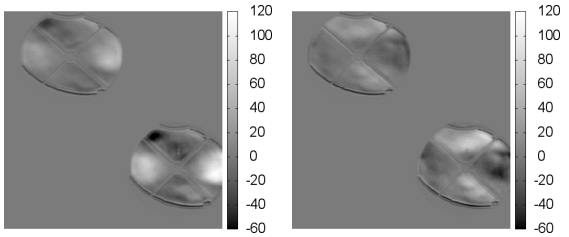

(a) (b)

Figure 14. Pupil intensity differences when observing a sunspot (Fig. 13) with trefoil aberrations at $+\,250$ nm RMS (a) and $-\,250$ nm RMS (b).

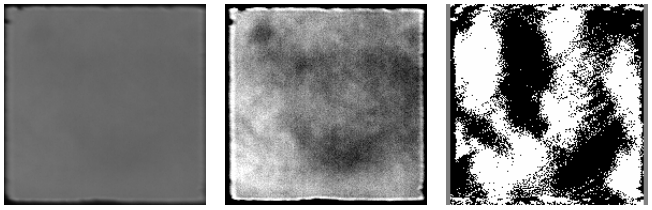

(a) (b) (c)

Figure 15. Observed solar granulation (a) with adjusted tone levels (b) and the horizontal mask (c).

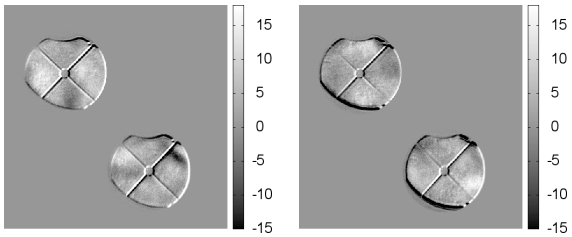

(a) (b)

Figure 16. Pupil intensity differences when observing solar granulation with astigmatism aberrations at $+\,150$ nm RMS (a) and $-\,150$ nm RMS (b).

extinction. When designing an OD-WFS based on a LCD, one has to consider optical diffraction, which duplicates the pupil image, caused be the pixel walls.

We were able to distinct several low order wavefront aberrations with our setups observing various target structures. We state the importance of the directions of the wavefront slopes, which are to be sensed, not being diagonal to a dominating structure in the observed object. Although we were not yet able to set up a calibrated wavefront measuring device, our experiments show that the concept of optical wavefront differentiation might be usefull for sensing the slopes of wavefronts emanating from extended incoherent sources. Future tests will have to show if the OD-WFS can be operated in closed loop of an AO system.

REFERENCES

1. O. von der Lühe, "Wavefront Error Measurement Technique Using Extended, Incoherent Light Sources," *Optical Engineering* **27**, pp. 1078–1087, 1988.
2. O. von der Lühe, "A wavefront sensor for extended, incoherent targets," in *Proceedings of the workshop on adaptive optics in solar observations*, *LEST Technical Report*, pp. 155–167, LEST Foundation, Dec. 1987.
3. J. D. Gaskill, *Linear Systems, Fourier Transforms and Optics*, John Willey & Sons, New York, 1978.
4. Seiko Epson Corporation, *3LCD Homepage*. http://www.3lcd.com/.
5. R. J. Noll, "Zernike polynomials and atmospheric turbulence," *Journal of the Optical Society of America* **66**, pp. 207–211, 1976.
6. W. H. Press, B. P. Flannery, S. A. Teukolsky, and W. T. Vetterling, *Numerical Recipes in C: The Art of Scientific Computing*, Cambridge University Press, Cambridge (UK) and New York, 2nd ed., 1992.
7. G. Vdovin and P. M. Sarro, "Flexible mirror micromachined in silicon," *Applied Optics* **34**, pp. 2968–2972, June 1995.
8. D. Schmidt, "Testaufbau eines neuen Sensors zur Bestimmung der Wellenfrontdeformation in optischen Sonnenteleskopen ," diploma thesis, Kiepenheuer Institut für Sonnenphysik, 2006.
9. O. von der Lühe, D. Soltau, T. Berkefeld, and T. Schelenz, "KAOS: Adaptive optics system for the Vacuum Tower Telescope at Teide Observatory," in *Innovative Telescopes and Instrumentation for Solar Astrophysics*, S. L. Keil and S. V. Avakyan , ed., **4853**, pp. 187–193, SPIE, Febuary 2003.